

IV. DISPERSION ESTIMATES AND GROUND-LEVEL SO₂ CONCENTRATIONS

A. Free Convection Scaling and the "Two-Thirds Law"

Deardorff's (1972) numerical modeling of the convective mixing layer showed that large convective eddies scale in size with H_m while turbulent velocities within this layer vary with the convective velocity scale w_* , given by

$$w_* = (qH_m)^{1/3} . \quad (14)$$

The appropriateness of H_m and w_* as the important length and velocity scales during strong convection was supported by laboratory simulations of turbulence in a water-filled convection chamber (Willis and Deardorff, 1974), wherein good agreement was found between these laboratory measurements and atmospheric observations. Recently, the convection chamber was used to simulate dispersion of neutrally buoyant particles into the mixed layer from a point source at a height of $0.25H_m$ (Willis and Deardorff, 1978). The nondimensional plume standard deviations, σ_y/H_m and σ_z/H_m , were given as functions of a nondimensional distance X , where

$$X = \frac{w_*}{v} \frac{x}{H_m} \quad (15)$$

i.e., the travel time x/v divided by H_m/w_* , a characteristic time scale for convective eddies in the mixed layer.

Lamb (1978a) conducted numerical simulations of neutrally buoyant particle diffusion from a point source into the mixed layer using the turbulence

velocity fields computed numerically by Deardorff (1974). The simulations for a source height of $0.26H_m$ were in excellent agreement with the laboratory results of Willis and Deardorff (1978). In a more recent paper, Lamb (1978b) investigated the dispersion characteristics for higher point source releases, at $0.5H_m$ and $0.75H_m$, and summarized his results into a simplified set of expressions. For release heights greater than $0.1H_m$, Lamb gave

$$\frac{\sigma_y}{H_m} = \begin{cases} \frac{1}{3} X, & \text{for } X < 1 \\ \frac{1}{3} X^{2/3}, & \text{for } 1 < X \leq 3 \end{cases} \quad (16a)$$

$$\frac{\sigma_z}{H_m} = \begin{cases} \frac{1}{2} X, & \text{for } X < 2/3 \\ \frac{1}{3}, & \text{for } X > 2/3 \end{cases} \quad (17a)$$

$$\quad \quad \quad (17b)$$

These results apply for v/w_* in the range

$$1.2 \leq \frac{v}{w_*} \leq 6.0 \quad (18)$$

The lower limit is imposed to ensure that diffusion along the plume axis can be ignored while the upper limit satisfies the condition that the bulk of the mixing layer be dominated by convective turbulence. (See Lamb, 1978b, for σ_y and σ_z expressions applicable to release heights less than $0.1H_m$.)

In the case of a buoyant stack plume dispersing in a convective mixing layer, we expect the plume standard deviations to be given by equations (16) and (17) far from the stack, where there are no longer stack buoyancy effects. Close to the stack, buoyancy-induced growth and rise should dominate the plume behavior. However, even near the stack, lateral meandering of the plume needs to be considered to predict σ_y for the time averaged plume.

The crosswind dispersion of a time averaged plume can be represented as

$$\sigma_y = (s_y^2 + m_y^2)^{1/2} \quad (19)$$

where s_y is the "relative" dispersion about the instantaneous plume centerline and m_y is the "meandering" of the centerline about its time averaged position (see Csanady, 1973). Close to the source s_y and m_y can be of the same order of magnitude while far from the source $s_y \gg m_y$. By "near" we mean for travel times $x/v < t_L$, where t_L is the Lagrangian integral time scale and by "far", we mean $x/v \gg t_L$. In a convective mixing layer $t_L \sim H_m/w^*$, and the travel time separating "near" and "far" is $x/v \sim H_m/w^*$ which is equivalent to $X \sim 1$.

Now consider buoyant plume dispersion in the region $X \leq 1$. We assume that the principal contribution to the "relative" dispersion is buoyancy-induced entrainment, and we have

$$s_y = \beta_{yL} z \quad (20)$$

where β_{yL} = the mean $\langle \sigma_y \rangle / z$ found earlier*

z = the rise above the stack.

Equation (20) should hold until the final rise Δh is reached. For distances beyond that to final rise, we assume that $s_y = \beta_{yL} \Delta h$. The "meandering" component of the dispersion, m_y , ought to vary linearly with travel time or distance for $X < 1$ according to statistical theory of turbulence (Taylor, 1921).

* For single stack plumes, we assumed $\beta_{yL} = 0.56$, which was the mean value found for $\langle \sigma_z \rangle / z$. This assumption was made because the calculated $\langle \sigma_y \rangle$'s were believed to be unrealistically large due to artificial low-level tails on the crosswind scattering ratio profile. (See discussion in Section III.A.) For the two-stack plumes, $\beta_{yL} = 0.35$.

Since Lamb's result (equation 16a) is consistent with statistical theory, we assume it to be representative of m_y for $X \leq 1$. The "total" dispersion can then be computed from equation (19) by replacing s_y by $\beta_{yL}z$ and m_y by $1/3 X$.

For dispersion in the region $X > 1$, we do not attempt to resolve the dispersion into "relative" and "meandering" components. In this region we are guided by the idea that σ_y should tend asymptotically to $1/3 X^{2/3}$ (equation 16b), and that there should be a smooth transition of σ_y in $X < 1$ to σ_y in $X > 1$. We also note that for strongly buoyant plumes which are still rising for $X > 1$, buoyancy-induced entrainment will continue to contribute to the "total" σ_y .

Consistent with the above discussion, the following formula is proposed for computing σ_y :

$$\frac{\sigma_y}{H_m} = \begin{cases} \left[2.6 \beta_{yL}^2 \left(\frac{F}{v w_*^2 H_m} \right)^{2/3} X^{4/3} + \frac{1}{9} X^2 \right]^{1/2}, & \text{for } X \leq 1 \quad (21a) \\ \left[2.6 \beta_{yL}^2 \left(\frac{F}{v w_*^2 H_m} \right)^{2/3} X^{4/3} + \frac{1}{9} X^{4/3} \right]^{1/2}, & \text{for } 1 < X. \quad (21b) \end{cases}$$

The first term within the brackets on the right hand side of equation (21) is $\beta_{yL}^2 z^2 / H_m^2$ in which z has been replaced by equation (1) to yield the $X^{4/3}$ dependence. The buoyancy-induced entrainment represented by this first term is assumed to increase only up until the final plume rise is reached. For $X \geq X_f$, where X_f is the nondimensional distance to final rise, the first term inside the brackets is assumed to be constant and evaluated at $X = X_f$. The second term inside the brackets is the square of the dispersion given by Lamb's

results (equation 16a is used for the second term in equation 21a and equation 16b for the second term in equation 21b). For two-stack operation, the sum of the buoyancy fluxes is used in equation (21).

Measured and predicted values of σ_y/H_m are in close agreement, as shown in Fig. 8. The solid lines are the average prediction curves (equation 21) for the different cases plotted and deviate from the individual curves (not shown) by less than 5 percent. Note that the solid curves differ from the Lamb prediction most significantly for $X < 1$, the region where plume rise and buoyancy-induced entrainment occur. For the cases shown, a typical distance to final plume rise is $X_f = 0.8$. Only cases meeting the criteria of equation (18) are used in this analysis.

Fig. 8 shows that the single stack data (Fig. 8a) tend to lie slightly above the solid curve, whereas the two-stack data (Fig. 8b) tend to lie somewhat below it. One possible explanation for these differences may be the different wind directions and surface heat transfer characteristics upwind of the stacks in the two situations. For the single stack data, the wind came from the north to north-northeast and the upwind fetch was a mixture of open fields and trees where we would expect strong convective activity during midday. This convective field would be transported some distance across the Potomac River before the cooler water surface, with its reduced surface (to air) heat flux, would diminish convective mixing. For the two-stack cases, the wind came either from the northwest or southwest and traversed a considerable stretch of water upwind of the plant. In this situation, we would expect reduced convective activity and a smaller w_* in the air approaching the power plant. This would lead to less lateral meandering and the smaller σ_y found in Fig. 8b.

The vertical plume standard deviation followed the prediction of the "two-thirds law" quite well out to the final rise distance (Fig. 7). For distances

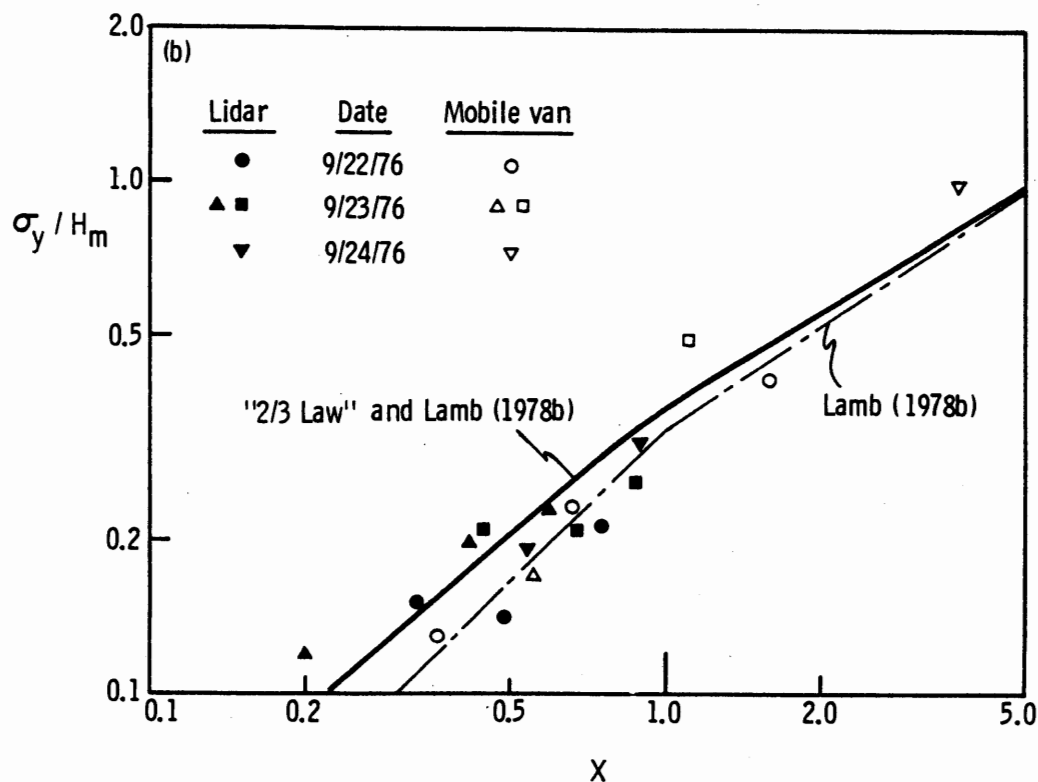
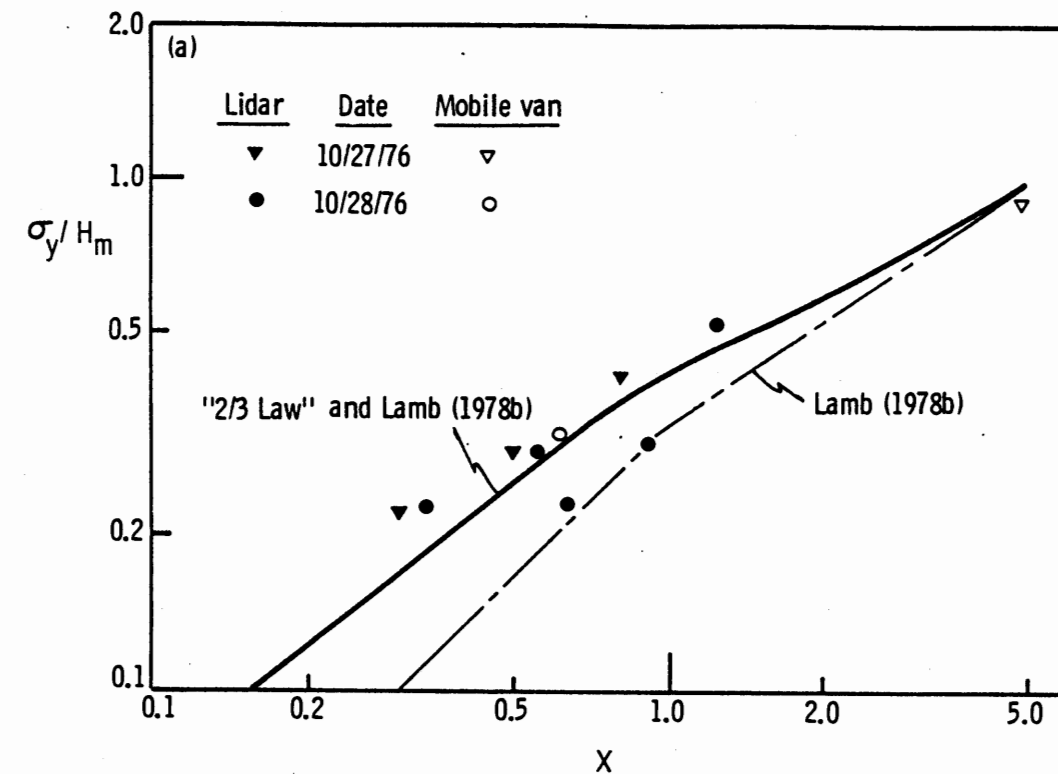


Figure 8. Nondimensional crosswind standard deviation as a function of nondimensional downwind distance. Measurements compared to predictions using combined "two-thirds law" and Lamb (1978b) and Lamb's (1978b) numerical results. a) single stack cases; b) two-stack cases. (Measurements approximate σ_y of hourly averaged plume.)

beyond X_f , the plume should behave as a passive tracer, diffusing according to Lamb's results and with an initial σ_z ($= \sigma_{zf}$), given by the value at X_f . The linear vertical spread with distance (equation 17a) given by Lamb is a good approximation to his numerical results for source height releases of $0.25H_m$ and $0.50H_m$. However, for a release height of $0.75H_m$ and $X > 0.15$, Lamb's detailed results show a slower variation of σ_z with distance ($\sigma_z \propto X^{0.77}$) due to the lower velocities in downdrafts at the top of the mixing layer. This slower growth results in a 30 percent smaller σ_z than that given by equation (17) at $X = 2/3$.

From the above discussion, we propose a simple tentative formula for σ_z for $X > X_f$:

$$\sigma_z = \sigma_{zf} \left(\frac{X}{X_f} \right)^\gamma, \quad X > X_f \quad (22)$$

where $\gamma = 0.77$ and 1 for effective stack heights above and below $\sim 0.63H_m$, respectively. (For $X < X_f$, $\sigma_z = \beta_z E^z$.) Equation (22) should hold only until the plume becomes uniformly distributed in the mixing layer. The limiting σ_z for a source at height h_e , is very far downstream,

$$\sigma_z = \left(\frac{1}{3} H_m^2 - h_e H_m + h_e^2 \right)^{1/2} \quad (23)$$

Lamb's approximate value for the limiting σ_z ($= 1/3H_m$) only differs by 15 percent from that given by equation (23) for h_e 's between $0.25H_m$ and $0.75H_m$.

Only five data points were taken beyond the final rise distance for comparison to the σ_z prediction given by equation (22). These are shown in Fig. 9 along with other σ_z measurements made during the same time interval but at distances less than X_f . Predictions given by the "two-thirds law"

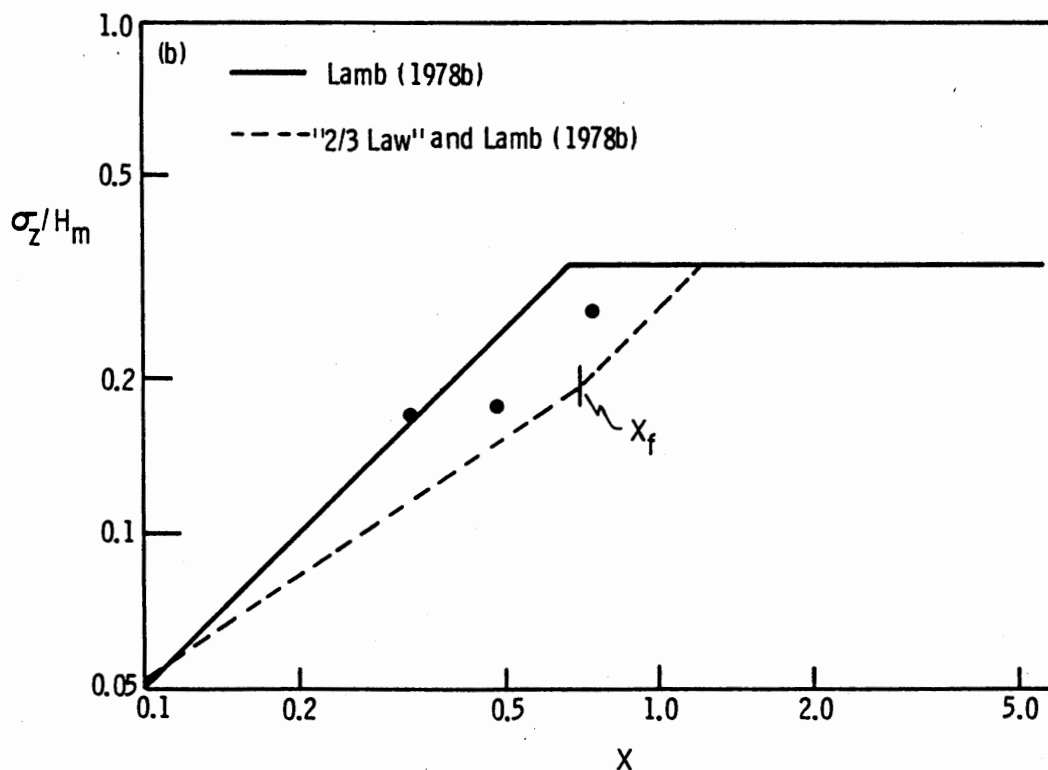
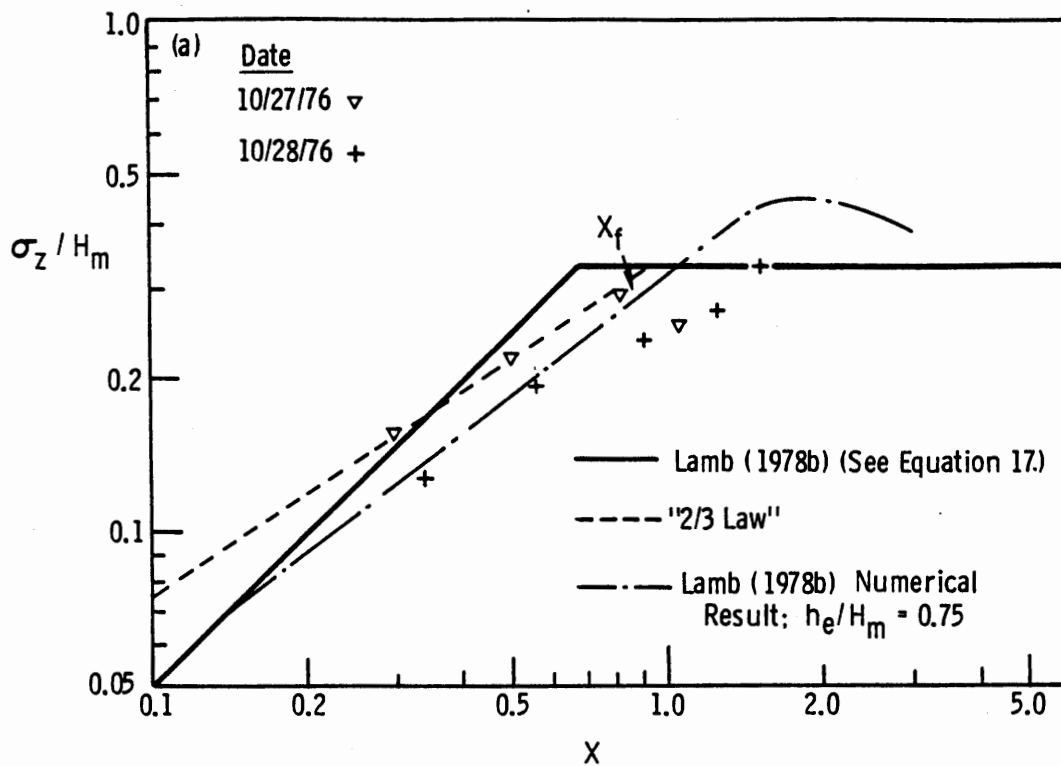


Figure 9. Nondimensional vertical plume standard deviation as a function of nondimensional downwind distance. Measurements compared to predictions of "two-thirds law" and Lamb (1978b). a) single stack cases, $h_e/H_m = 0.70$; b) two-stack cases, $h_e/H_m = 0.61$. (Measurements approximate σ_z of hourly averaged plume.)

and equation (21) are shown out to X_f and beyond X_f , respectively. The data are in rough agreement with these predictions. Equation (17) (solid curve in Fig. 9) shows more rapid spreading than the "two-thirds law" prediction and generally predicts higher σ_z 's than were observed. Lamb's numerical result (dash - dot curve) for $h_e/H_m = 0.75$ agrees roughly with the single stack data (Fig. 9a) where $h_e/H_m = 0.7$.

Two straightforward improvements in the σ_z prediction should be made. First, Lamb's σ_z should be resolved into the contribution due to vertical displacement of the plume centroid and that due to dispersion about the centroid. Only the latter contribution should be used in combination with the buoyant plume dispersion since vertical displacement of the buoyant plume centroid is treated separately by the rise formulas discussed earlier. (The data were not available in this study for the resolution of Lamb's σ_z into the above mentioned components.) Second, vertical meandering of the plume centroid during plume rise should be considered as a possible additional contribution to σ_z and treated as for σ_y . Although this was not necessary in the present analysis (in view of the good correlation in Fig. 7), the present data were collected when w_*/v was typically 0.25. For stronger convection where w_*/v might be 0.5 or greater, vertical meandering would play a more significant role in the time-averaged σ_z .

Calculations of ground-level SO_2 concentrations have been made using the Gaussian plume model with the above predicted σ_y and σ_z . To compute the effective stack height, we used the lowest plume rise given by the three following methods: the prediction of the "two-thirds law" at the measurement distance, the 1975 Briggs plume rise formulas (equations 9, 10, and 11), or the height of a trapped plume (equation 13). Calculated concentrations are compared to measured SO_2 values in Table 3. For the most part, the two are

Table 3. Comparison between calculated and observed ground-level SO₂ concentrations

Date	Time	x (m)	C _{2 meas} [*] (ppb)	"Two-Thirds Law" and Lamb		Brookhaven, Weil (1974) Algorithm				Pasquill, Turner (1964) Approach Drop 1 stability class				
				C _{pred} (ppb)	$\frac{C_{pred}}{C_{2 meas}}$	Brookhaven Stability Class	C _{pred} (ppb)	$\frac{C_{pred}}{C_{2 meas}}$	$\frac{x}{x_{max}}$	Pasquill Stability Class †	C _{1 meas} ^{**} (ppb)	C _{pred} (ppb)	$\frac{C_{pred}}{C_{1 meas}}$	$\frac{x}{x_{max}}$
9/22/76	1047	2401	9	3	0.33	B ₁	59	6.60	0.63	B	18	15	0.83	0.52
9/22/76	1359	8918	37	49	1.33	B ₁	45	1.22	1.78	C	50	36	0.72	0.81
9/22/76	1645	4115	15	9	0.60	B ₁	32	2.11	0.62	C	32	0.10	0.003	0.29
9/23/76	1320	5694	76	64	0.84	B ₁	62	0.81	1.08	C	90	12	0.13	0.52
9/23/76	1524	3180	10	8	0.80	B ₁	38	3.80	0.59	C	18	0.05	0.003	0.29
9/24/76	1154	12,271	45	105	2.33	B ₂	49	1.10	4.02	A	63	56	0.89	7.48
10/27/76	1509	25,523	15	16	1.07	B ₁	13	0.87	4.06	C	16	20	1.25	1.95
10/28/76	1607	3905	16	30	1.88	B ₁	29	1.81	0.65	B	30	13	0.43	0.59

* C_{2 meas} = Maximum SO₂ concentration from average crosswind profile; approximately a 1-hour average.

** C_{1 meas} = Average of peak SO₂ concentration from repeated passes; approximately a 10-minute average.

† Pasquill stability class after the shift in stability condition.

in good agreement.* A summary of comparisons between measured and predicted σ_y , σ_z , and SO_2 concentrations is given in Table 4 (see "two-thirds law" and Lamb). Predictions based on free convection scaling and the "two-thirds law" agreed better with observations than those using empirical dispersion estimates (discussed below).

B. Empirical Dispersion Estimates

Measured plume dispersion and SO_2 concentrations have also been compared to predictions based on the Brookhaven sigma curves using Weil's (1974) algorithm. The measured plume standard deviations are somewhat less than the Brookhaven B1 class predictions shown in Fig. 10 (see also summary in Table 4). Calculated ground-level concentrations using the Brookhaven dispersion estimates in the Gaussian model exceeded the measurements, on the average, by a factor of 1.76 (geometric mean). This is attributed to measurements made at distances less than x_{max} , the distance to maximum concentration. In four cases where $x \sim 0.6 x_{\text{max}}$ (Table 3), the geometric mean of $c_{\text{pred}}/c_{\text{meas}}$ is 3.1 while the geometric mean of $c_{\text{pred}}/c_{\text{meas}}$ for $x > x_{\text{max}}$ is 0.99. Concentrations close to the stacks were predicted to be higher than the observed because the vertical plume dispersion is overestimated.

Measured and calculated plume dispersions based on the Pasquill, Gifford, Turner (PGT) approach are compared in Fig. 11 for measurements falling in the neutral (Pasquill D) stability class. The PGT approach was tried both with the stability class selected for the prevailing meteorological conditions, and also with the next more unstable class. The σ_y predictions are in fair

* Predicted concentrations are within a factor of 2 of the measurements.

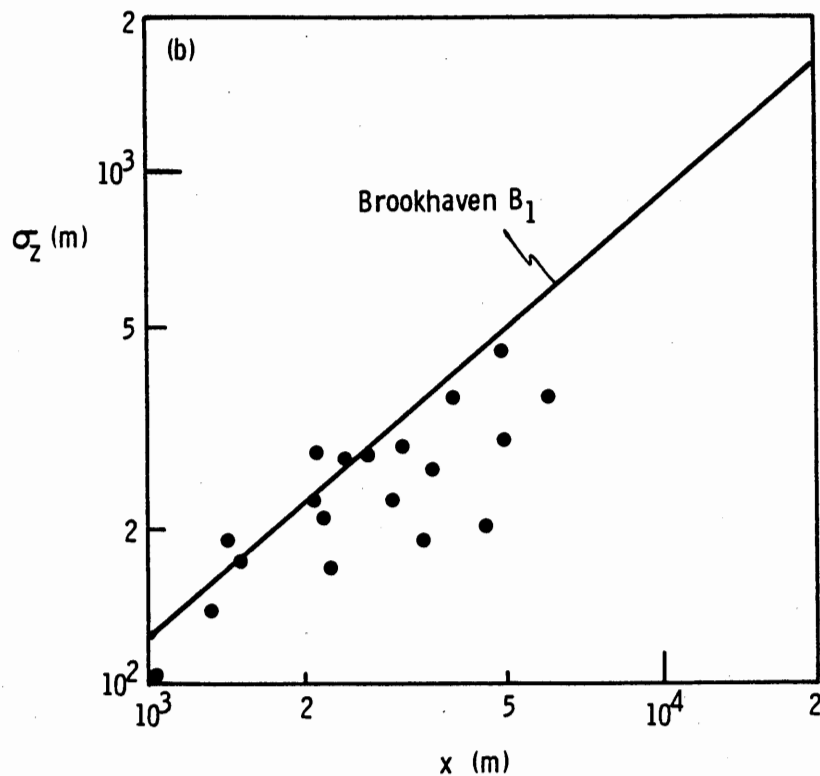
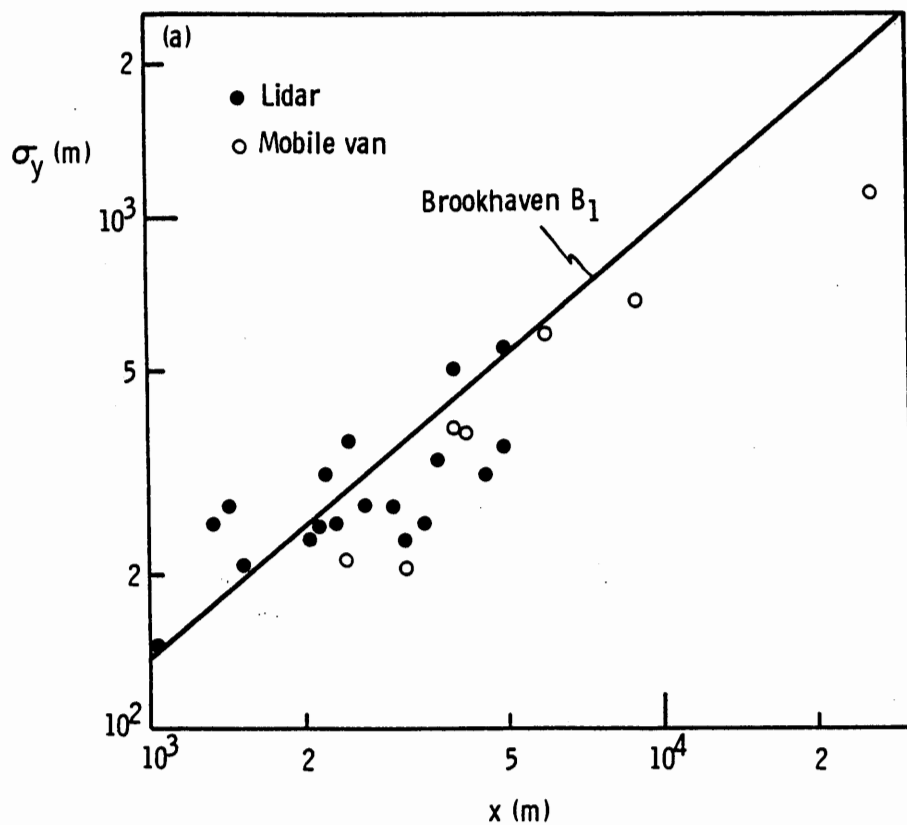


Figure 10. Measured plume standard deviations as a function of distance compared to predictions of Brookhaven B_1 stability class; stability class selected using Weil (1974) algorithm. a) crosswind standard deviation; b) vertical standard deviation. (Measurements approximate σ_y and σ_z of hourly averaged plume.)

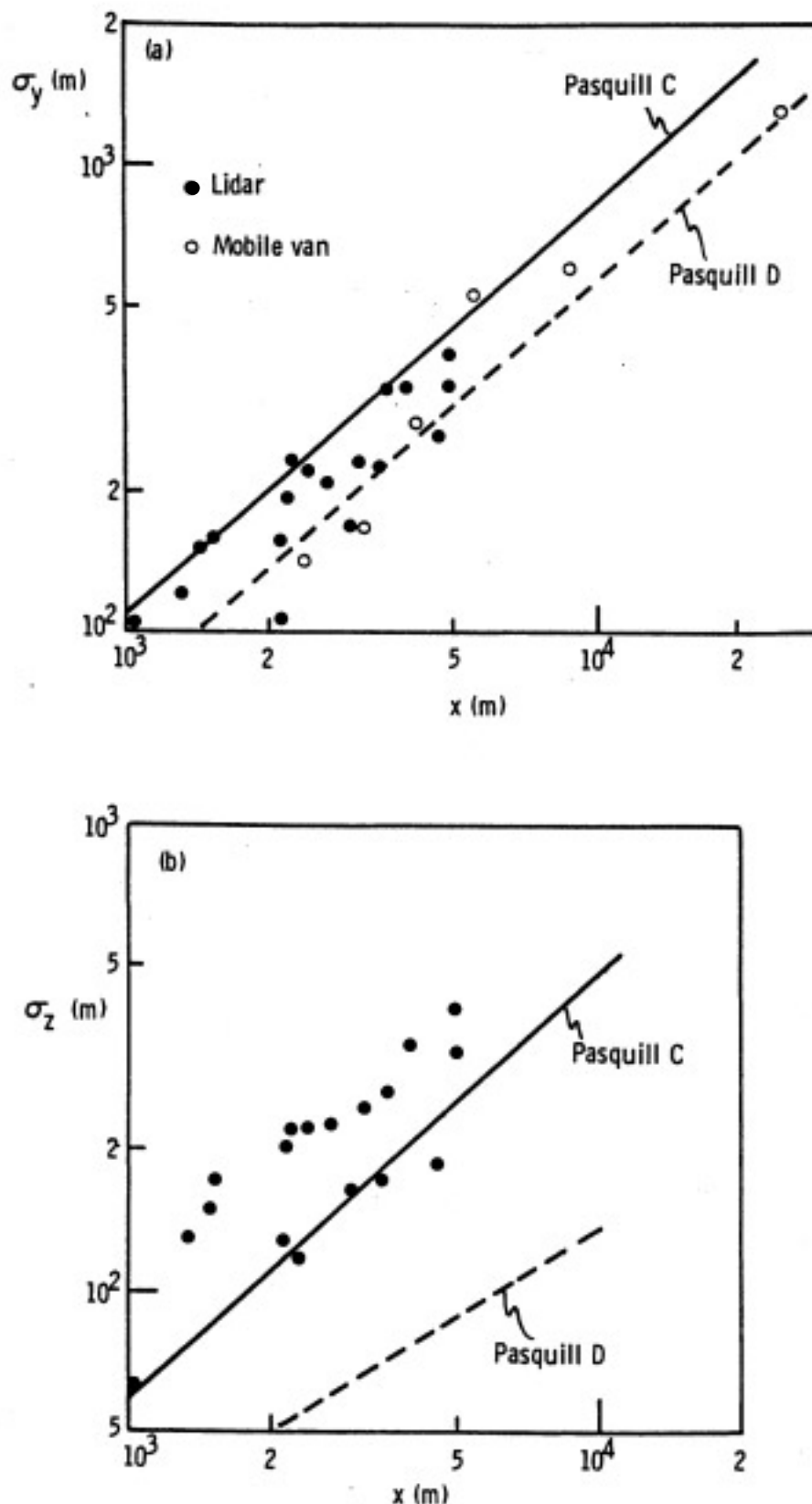


Figure 11. Measured plume standard deviations as a function of distance compared to predictions of Pasquill-Gifford C and D sigma curves. All measurements correspond to neutral (D class) stability as determined by Turner (1964) approach. a) crosswind standard deviation; b) vertical standard deviation. (Measurements approximate σ_y and σ_z of 10-minute averaged plume.)

Table 4. Summary of comparisons between observed and calculated σ_y , σ_z , and ground-level SO_2 concentrations

Ratio	"Two-Thirds Law" and Lamb	Brookhaven-Weil (1974) Algorithm	Pasquill-Turner (1964); Drop One Stability Class	Pasquill-Turner (1964) Approach	Number of Cases*
$\frac{\sigma_y \text{ meas}^{**}}{\sigma_y \text{ pred}}$	0.94 ± 0.19	0.89 ± 0.25	0.74 ± 0.19	1.09 ± 0.29	26
$\frac{\sigma_z \text{ meas}^{**}}{\sigma_z \text{ pred}}$	0.91 ± 0.18	0.81 ± 0.21	1.27 ± 0.46	3.08 ± 1.05	18
$\frac{c_{\text{pred}}}{c_{\text{meas}}} \dagger$	0.98 (1.87)	1.76 (2.09)	0.16 (12.54)		8

* Each case represents an average of repeated measurements. Data used in analysis of the "two-thirds law" and Lamb and Brookhaven-Weil approach approximate 1-hour averages; data used for comparison to the Pasquill-Turner approach approximate 10-minute averages.

** Ratios are arithmetic means \pm one standard deviation.

† Top ratio is geometric mean; bottom value in parentheses is geometric standard deviation.

agreement with the measurements, being somewhat better for the Pasquill D class curve (see Table 4). However, measured σ_z 's are about a factor of 3 higher than the class D predictions and even somewhat higher than the class C curve. The underestimated σ_z 's result in overestimates of the distance x_{\max} and explain why predicted ground-level concentrations using the PGT approach in the Gaussian model underestimate measured concentrations close to the stacks ($x < x_{\max}$), as shown in Table 3 (Pasquill stability class dropped by one). Predicted concentrations using the unmodified PGT approach (no shift in stability class) generally were several orders of magnitude less than measured values and are not shown in Table 3.

The results found here using the empirical dispersion estimates are generally consistent with those found in earlier studies of stack plume dispersion at Maryland power plants (Weil, 1974, 1977). Further discussion of reasons for differences between the measurements and predictions is given by Weil (1978).

V. CONCLUSIONS

Lidar measurements of the rise and growth of plumes from the Morgantown power plant stacks were used to assess plume rise and dispersion models.

The following conclusions were drawn:

1. Plume-borne aerosols were found to be good tracers of stack-emitted SO_2 . The shape and width of the aerosol profiles obtained by lidar were similar to SO_2 profiles obtained with a Barringer correlation spectrometer in a mobile van.
2. The observed initial plume rise with two stacks operating showed a rise enhancement relative to observed rise with only one stack operating. Observed rise with two stacks operating was close, on the average, to predictions given by the "two-thirds law" using the sum of the buoyancy fluxes from the two stacks. Initial observed rise with one stack operating agreed well with predictions of the "two-thirds law."
3. The instantaneous crosswind and vertical dispersions and the time-averaged, vertical dispersion during initial rise of the buoyant plume were linearly proportional to rise as given by the "two-thirds law", but the proportionality constants were different for the single and two-stack plume observations. A significant feature of these measurements is that they extended almost 5 km downwind of the stacks.
4. Briggs' (1975) formulas for turbulence-limited final rise in neutral or convective conditions agreed well with measurements of turbulence-limited final rise and with all measured maximum plume rises. The lowest predicted final rise from three formulas, one for neutral conditions (equation 9), and two for convective situations (equations 10 and 11), was chosen as the best estimate of final rise; the conclusion given here is based on the comparison between the lowest predicted rise and the observed rise in each case.
5. Briggs' (1970) model for final rise in neutral conditions consistently underestimated measurements of turbulence-limited final rise and all measured maximum plume rises. The lower of the rise predictions from Briggs' original formulation (equations 3 and 4) and Weil's (1974) modification to it (equations 3 and 7) was chosen as the best estimate of a final rise. Briggs' original formulation gave a lower estimate of final rise in all cases.
6. A combination of the dispersion predictions from the "two-thirds law" and Lamb's (1978b) results for diffusion of neutrally buoyant particles in convective mixing layers yielded dispersion estimates that agreed well with observations. Ground-level SO_2 concentrations predicted using the Gaussian model and the above procedure for computing σ_y and σ_z were equal, on the average, to observed SO_2 concentrations; the geometric standard deviation of the ratio of predicted-to-measured

concentration was 1.9. Dispersion predictions using the "two-thirds law" and Lamb's results also agreed better with observations than estimates given by the Brookhaven-Weil (1974) or the Pasquill, Gifford, Turner (1964) methods.

VI. REFERENCES

- Briggs, G.A. 1969. Plume Rise. U.S. Atomic Energy Commission, TID-25075, 81 pp.
- Briggs, G.A. 1970. Some recent analyses of plume rise observations. Paper presented at 2nd International Clean Air Congress. Washington, D.C., Paper No. ME-8E.
- Briggs, G.A. 1974. Plume rise from multiple sources. Air Resources, Atmospheric Turbulence and Diffusion Laboratory, National Oceanographic and Atmospheric Administration. Oak Ridge, Tennessee, ATDL No. 91.
- Briggs, G.A. 1975. Plume rise predictions. In Lectures on Air Pollution and Environmental Impact Analyses, American Meteorological Society, Boston, Mass., pp. 59-111.
- Browell, E.V. 1977. Lidar remote sensing of tropospheric pollutants and trace gases - programs of NASA Langley Research Center. In proceedings of Fourth Joint Conference on Sensing of Environmental Pollutants, New Orleans, La., November 6-11, 1977.
- Csanady, G.T. 1973. Turbulent Diffusion in the Environment. D. Reidel Publishing Co., Boston, Mass. 248 pp.
- Deardorff, J.W. 1972. Numerical investigation of neutral and unstable planetary boundary layers. J. Atmos. Sci. 29:91-115.
- Deardorff, J.W. 1974. Three-dimensional study of the height and mean structure of a heated planetary boundary layer. Boundary Layer Met. 7:81-106.
- Engineering Test Services. 1977. Source testing for the lidar evaluation at the PEPCO Morgantown generating station, Morgantown, Maryland, September - October 1976. Report by Engineering Test Services, Sandston, Va.
- Hamilton, P.M. 1967. "Paper III: Plume height measurements at Northfleet and Tilbury power stations." Atmos. Environ. 1:379-387.
- Johnson, W.B. and Uthe, E.E. 1971. Lidar study of the Keystone stack plume. Atmos. Environ. 5:703-724.
- Lamb, R.G. 1978a. A numerical simulation of dispersion from an elevated point source in the convective planetary boundary layer. Atmos. Environ. 12:1297-1304.
- Lamb, R.G. 1978b. The effects of release height on material dispersion in the convective planetary boundary layer, Draft, Division of Meteorology, U.S. Environmental Protection Agency, Research Triangle Park, N.C.

- Mills, R.S., Allen, R.J., and Butler, C.F. 1978. An experimental/analytical program to assess the utility of lidar for pollution monitoring, Prepared by Department of Physics and Geophysical Sciences, Old Dominion University, Norfolk, Va., Technical Rept. PG STR-AP 78-9.
- Taylor, G.I. 1921. Diffusion by continuous movements. Proc. London Math. Soc. 20:196-212.
- Turner, D.B. 1964. A diffusion model for an urban area. J. Appl. Meteor. 3:83-91.
- Weil, J.C. 1974. Comparison between measured and model-estimated ground-level SO₂ concentrations downwind from the Dickerson Power Plant, prepared by Martin Marietta Laboratories for Maryland Power Plant Siting Program, Department of Natural Resources, Ref. No. PPSP-MP-11.
- Weil, J.C. 1977. Evaluation of the Gaussian plume model at Maryland power plants, prepared by Martin Marietta Environmental Technology Center for Maryland Power Plant Siting Program, Department of Natural Resources, Ref. No. PPSP-MP-16.
- Weil, J.C. 1978. Applicability of stability classification schemes and associated parameters to dispersion of tall stack plumes in Maryland. Submitted to Atmos. Environ.
- Weil, J.C. and Jepsen, A.F. 1977. Evaluation of the Gaussian plume model at the Dickerson Power Plant. Atmos. Environ. 11:901-910.
- Willis, G.E. and Deardorff, J.W. 1974. A laboratory model of the unstable planetary boundary layer. J. Atmos. Sci. 31: 1297-1307.
- Willis, G.E. and Deardorff, J.W. 1978. A laboratory study of dispersion from an elevated source within a modeled convective planetary boundary layer. Atmos. Environ. 12:1305-1312.

APPENDIX A

Data Used In Analysis

Nomenclature for Tables A1 - A6

A. Lidar Backscatter and SO₂ Profile Results (Tables A1 and A4)

RUN = an identification code for each set of lidar (or SO₂) profiles and associated meteorological and power plant conditions

START TIME = time at which repeated lidar scans or mobile van traverses began for a particular cross section; first two digits are the hour, last two digits are minutes after the hour

END TIME = time at which repeated scans or van traverses ended for a cross section

x = radial distance from power plant to the centroid of the average scattering ratio (SR) lidar distribution or the average crosswind SO₂ profile; average profile computed from N repeated scans or traverses (m)

z = height of centroid of average lidar SR distribution above the stack (m)

σ_y = crosswind standard deviation computed from average lidar SR distribution or average crosswind SO₂ profile (m)

σ_z = vertical standard deviation computed from average lidar SR distribution (m)

$\langle \sigma_y \rangle$ = average of N individual crosswind standard deviations from repeated lidar scans or repeated SO₂ profiles at a cross section (m)

$\langle \sigma_z \rangle$ = average of N individual vertical standard deviations from repeated lidar scans at a cross section (m)

N = number of lidar scans or SO₂ profiles in a set of repeated measurements at a cross section

PHI = angular bearing of centroid of average crosswind SO₂ profile; angle measured clockwise from grid north (deg)

c_2 = maximum SO₂ ground-level concentration from average crosswind SO₂ profile (ppb)

std₂ = standard deviation in SO₂ concentration about c_2 (ppb)

c_1 = average of individual maximum SO₂ ground-level concentrations from N repeated crosswind profiles at a cross section (ppb)

std₁ = standard deviation in SO₂ concentration about c_1 (ppb)

B. Power Plant Operating Conditions (Tables A2 and A5)

Q_1, Q_2 = SO_2 emission rate for stack 1 and stack 2, respectively, computed from fuel consumption and fuel analysis (composition) data (kg/sec)

F_1, F_2 = buoyancy flux from stack 1 and 2, respectively, Briggs (1970) definition of buoyancy flux (m^4/sec^3).

C. Meteorological Conditions (Tables A3 and A6)

v = average wind speed in mixing layer (m/sec)

THETA = average wind direction in mixing layer; direction from which wind blows; direction measured clockwise from grid north (deg)

T_1 = average ambient temperature at surface ($^{\circ}C$)

DTDZ = average potential temperature gradient between stack top and top of mixing layer ($^{\circ}C/m$)

H_m = depth of mixing layer (m)

Q_R = solar insolation ($cal/cm^2/hr$)

HR = hour at which surface meteorological observations were obtained from airport weather data

CLC = cloud cover in tenths from airport weather data

CEL - ceiling height; unlimited ceiling height given by 999 (hundreds of feet)

VS = surface wind speed at airport (m/sec)

Table A1. Lidar measurements.

Date			Run	Start Time	End Time	x	Bulerian Averages			Arithmetic Mean		N	
Day	Mon.	Year					z	σ_y	σ_z	$\langle \sigma_y \rangle$	$\langle \sigma_z \rangle$		
22	9	76	2L	1558	1619	3210	192	241	222	227	153	10	
22	9	76	3L	1638	1744	2152	608	242	286	158	204	6	
				1630	1748	3162	792	236	291	230	246	8	
				1648	1751	4888	736	354	448	313	386	6	
23	9	76	5L	1337	1410	2287	294	252	167	232	117	8	
				1338	1411	3471	325	251	189	225	172	7	
				1340	1412	4564	485	314	201	262	186	8	
23	9	76	6L	1529	1604	1004	262	143	104	98	62	7	
				1531	1607	2137	352	236	226	104	129	7	
				1530	1608	2979	502	274	229	167	166	14	
24	9	76	8L	1253	1335	1524	540	211	175	168	171	5	
				1255	1337	2527	657	343	187	315	176	5	
15	10	76	9L	1142	1158	1142	140	84	88	69	75	14	
15	10	76	10L	1217	1236	2114	286	192	130	184	103	9	
15	10	76	11L	1354	1454	415	71	60	46	76	34	8	
				1356	1455	1544	170	115	117	132	105	9	
				1358	1501	2506	225	213	177	192	150	19	

Table A1. (cont'd.)

Date			Run	Start Time	End Time	x	Bulerian Averages			Arithmetic Mean		N
Day	Mon.	Year					z	σ_y	σ_z	$\langle \sigma_y \rangle$	$\langle \sigma_z \rangle$	
26	10	76	12L	1700	1801	841	124	210	85	291	70	11
				1702	1806	2036	179	243	115	212	90	10
				1704	1808	3207	254	279	140	235	139	10
				1705	1810	4422	246	367	160	300	170	9
27	10	76	13L	1433	1547	1429	353	271	192	265	151	4
				1435	1550	2421	535	362	275	232	223	4
				1440	1610	3941	636	510	360	386	338	6
				1443	1614	5121	527	260	308	220	306	3
28	10	76	14L	1025	1113	1342	169	254	139	245	130	6
				1027	1135	2211	293	317	212	324	222	7
				1030	1138	3659	456	334	261	343	269	7
				1034	1147	4951	553	568	300	514	324	7
				1036	1154	6074	528	383	365	428	373	7
28	10	76	15L	1516	1632	2682	456	276	282	207	229	10

Table A2. Meteorological conditions for lidar data

Day	Month	Year	Run	v	THETA	T ₁	DTDZ	H _m	Q _R	HR	CLC	CEL	VS
22	9	76	2L	13.7	306	18	0.0	1650	48.0	16	0	999	6.2
22	9	76	3L	6.7	298	18	0.0	1650	30.0	16	0	999	6.2
23	9	76	5L	8.4	222	24	0.0	1200	61.8	13	5	999	7.7
23	9	76	6L	7.3	211	21	0.0	1200	43.2	16	8	999	8.8
24	9	76	8L	4.3	50	19	0.0018	1100	42.9	13	8	999	3.6
15	10	76	9L	10.8	228	19	0.0	700	63.6	13	0	999	9.3
15	10	76	10L	10.0	224	19	0.0	700	64.2	13	0	999	9.3
15	10	76	11L	12.1	234	23	0.0008	1200	56.4	16	0	999	7.2
26	10	76	12L	11.9	358	7	0.008	1250	7.2	19	0	999	9.3
27	10	76	13L	5.8	1	3	0.0013	1250	27.1	16	10	100	7.2
28	10	76	14L	6.2	12	5	0.0003	1100	46.2	10	6	999	5.1
28	10	76	15L	5.5	313	5	0.0008	1200	33.0	16	2	999	4.1

Table A3. Plant conditions for lidar data

Day	Month	Year	Run	Q ₁	F ₁	Q ₂	F ₂
22	9	76	2L	1.73	737	1.70	724
22	9	76	3L	1.73	741	1.73	741
23	9	76	5L	1.74	704	1.63	704
23	9	76	6L	1.75	723	1.65	723
24	9	76	8L	1.69	724	1.76	736
15	10	76	9L			1.65	741
15	10	76	10L			1.64	742
15	10	76	11L			1.61	717
26	10	76	12L			1.79	819
27	10	76	13L			2.02	843
28	10	76	14L			2.04	831
28	10	76	15L			2.06	825

Table A4. Mobile van measurements.

Date			Run	Start Time	End Time	x	PHI	Ground-level SO ₂ Profiles								Vertically Integrated SO ₂ Profiles		
								Average Profile			Arithmetic Means					Average Profile σ_y	Arithmetic Mean $\langle \sigma_y \rangle$	
Day	Month	Year						c ₂	std ₂	σ_y	c ₁	std ₁	$\langle \sigma_y \rangle$	N				
22	9	76	1W	1047	1215	2401	130	9	17	495	18	19	468	8	214	140		
			2W	1359	1522	8918	117	37	36	670	50	31	464	6	688	602		
			3W	1645	1736	3441	110	15	15	525	32	17	281	4	389	290		
23	9	76	4W	1320	1414	5694	28	76	90	426	90	81	417	4	595	532		
			5W	1524	1609	2734	32	10	14	262	18	18	134	6	196	159		
24	9	76	6W	1154	1306	12271	207	45	32	2484	63	38	1284	5	1112	966		
27	10	76	7W	1509	1554	25523	162	15	1	2138	16	1	1922	3	NA*	NA		
28	10	76	8W	1607	1642	2221	116	16	26	775	30	29	318	6	388	320		

*NA profiles were not measured because integrated SO₂ levels were below the sensitivity of the correlation spectrometer.

Table A5. Meteorological conditions for mobile van data

Day	Month	Year	Run	v	THETA	T ₁	DTDZ	H _m	Q _R	HR	CLC	CEL	VS
22	9	76	1MV	9.4	309	17	0.0	1650	69.0	10	1	999	7.2
			2MV	7.6	299	20	0.0	1650	68.4	16	0	999	6.2
			3MV	6.7	298	20	0.0	1650	35.0	16	0	999	6.2
23	9	76	4MV	8.4	224	24	-0.0012	1200	63.8	13	5	999	7.7
			5MV	7.2	211	21	-0.0020	1200	46.8	16	8	999	8.8
24	9	76	6MV	4.6	59	20	-0.0020	1100	49.8	13	8	999	3.6
27	10	76	7MV	5.8	1	3	0.0010	1250	22.2	16	10	100	7.2
28	10	76	8MV	5.5	313	5	0.0	1200	33.0	16	2	999	4.1

Table A6. Plant conditions for mobile van data

Day	Month	Year	Run	Q ₁	F ₁	Q ₂	F ₂
22	9	76	1MV	1.72	750	1.67	754
			2MV	1.73	723	1.40	601
			3MV	1.73	727	1.73	728
23	9	76	4MV	1.74	705	1.66	705
			5MV	1.74	721	1.65	723
24	9	76	6MV	1.72	722	1.78	730
27	10	76	7MV			1.64	718
28	10	76	8MV			1.61	718

APPENDIX B

Comparison Between Crosswind Profiles of Scattering Ratio and SO₂

by

Jonathan L. Altman

One of the objectives of this study was to evaluate the usefulness of the lidar for inferring SO₂ distributions in buoyant stack plumes. The first step in such an evaluation is to compare data obtained with the lidar to similar data obtained by some other method. We have chosen to use the vertically integrated SO₂ distribution in the plume measured by a Barringer correlation spectrometer (COSPEC) for the comparison. We have routinely used that instrument in the past to obtain information about the SO₂ distribution of the elevated plume. The lidar backscatter data can be processed to give the vertically integrated scattering ratio in sections through the plume. As discussed in the footnote on page II-3, the scattering ratio is a measure of the relative particulate mass concentrations in the plume.

In making the comparison between these two sets of data, two basic assumptions were made. First, we assumed that the settling velocities of the particles in the plume were small enough that the particulates were dispersed in the same way as a gas. Second, we assumed that the proportion of suspended particulates to SO₂ gas in the stack effluent was constant during the time required for one set of lidar and COSPEC measurements. Both these assumptions require close scrutiny in the light of the results of the comparison.

The lidar and COSPEC measurements were compared for five sets of simultaneously taken data. Dates and configurations under which these data sets were taken are given in the first four columns of Table B1 and in the maps of Figures B1 to B4. Since a single crosswind profile takes longer to obtain

with the COSPEC than with the lidar, because of the van's travel time, we have made no attempt to directly compare individual crosswind profiles; instead, an averaged profile for the time periods indicated was calculated. The results were then compared on the basis of (1) the shapes and widths of the profiles (qualitative comparison), (2) the crosswind standard deviations (σ_y) (quantitative comparison), and (3) locations of the centroid of the vertically integrated concentration distributions.

The lidar data were initially analyzed to give the vertically integrated scattering ratio as a function of distance along the lidar line of sight for each lidar scan. The distance along this line was then divided into 200-meter segments, and the integrated scattering ratios falling within each segment were summed. The sums for a given segment from each of the individual profiles within a given time period were then averaged, and each of the averages was divided by the maximum average value obtained for all the segments. Thus, an average profile normalized to unity at its peak was obtained for the appropriate time interval. Since the scattering ratio is proportional to the concentration of aerosols, the normalized profile just described is effectively a normalized concentration profile of aerosols. This profile was compared with a similarly normalized averaged COSPEC concentration profile of SO_2 over the same run. The standard deviations of each of the segmental averages were also computed and were normalized by the average scattering ratio for the appropriate segment.

The vertically integrated SO_2 concentration, or SO_2 burden, obtained by the COSPEC was analyzed similarly to the lidar data. For each individual SO_2 profile, the SO_2 burden was summed within the same crosswind segments used for computing the scattering ratio "sums". Fig. B1 illustrates this geometry. Normalized averages and standard deviations of the SO_2 burden "sums" were then computed for each crosswind segment by the same method used for the computation

of the lidar profiles. Plots of these normalized average "sums" and their standard deviations for both the lidar and COSPEC measurements are shown in Figs. B5 through B9.

A visual comparison of the profiles in Figs. B5 through B9 reveals fair overall agreement. The most obvious differences between the lidar and COSPEC profiles seem to be their relative displacement rather than any great differences in shape (with the exception of Fig. B8). The best agreement was obtained for the two profiles on 22 September.

Table B1 summarizes several parameters which give a quantitative measure of the crosswind dispersion, as well as the variability of the plume position during the measurement time. We found that, in every case, σ_y of the individual COSPEC profiles was greater than that for the lidar profile. This was also true in all but one case (25 Sept.; 1524-1609) for the σ_y of the averaged profile. The difference may be related to the difference in sampling time for the two instruments. The typical time required for a lidar scan is 1 minute, while the van carrying the COSPEC requires 3 to 5 minutes to complete a single pass under the plume.

The variation of the plume position is expressed in columns seven and eight of Table B1 as the standard deviation in both degrees and meters of the crosswind position of the centroids of the individual profiles. These values were calculated by taking the second moment of the angular position of the individual centroids about the mean centroid position. The lidar and COSPEC data show a marked disagreement in calculations of this parameter; however, the difference is not consistent as it was for the σ_y computations. It should be noted, however, that the two sets of data taken by the same method on the same day are consistent. Thus, both sets of COSPEC measurements on 23 September show a less variable plume than do the lidar, while the reverse

is true on 22 September. A closer examination of individual lidar profiles on the afternoon of 23 September revealed a fairly large variation in the scattering ratio profiles both horizontally and vertically. In addition, the wind profiles from that time period showed relatively large wind direction shear ($\sim 0.035^\circ/\text{m}$).

Although our data were not sufficiently detailed to indicate with any certainty the reasons for the differences between the lidar and the COSPEC measurements, there are several likely causes. We feel that the most important reason for the discrepancies is the difference in cross-section sampling time for the lidar and the COSPEC. In most cases, COSPEC profiles would be expected to be somewhat wider than the lidar profiles because of the wandering of the plume during the longer measurement time. This wandering would also affect the measures of plume variation (σ_y and plume centroid location) and depends on the time scale of the largest atmospheric eddies. Thus, the effects of time differences during cross-section sampling vary with the meteorological conditions (ambient turbulence time scale). Another factor which may have caused a difference between the lidar and COSPEC measurements is the possibility that the proportion of aerosol to SO_2 in the plumes was not always constant. Based on visual observations and the stack test data, we suspect that the stack particulate flux over short time intervals (several minutes) varied much more than the stack SO_2 flux. Constant stack fluxes of SO_2 and particulates during the measurements would be highly desirable in any future work.

Table B1. Computed plume parameters from lidar and COSPEC data

	Date	Time	No. of Indiv. Profiles	Centroid Distance From Stacks (m)	σ_y of Avg Profile (m)	Avg of σ_y Indiv. Profile (m)	Std. Dev. of Centroid Crosswind Pos. (m)	Std. Dev. of Centroid Crosswind Pos. (Deg)	Centroid Angular Pos. (Deg. from North)
COSPEC	9/22	1557-1638	4	3441	387	260	259	4.32	108
Lidar	9/22	1558-1619	10	3210	241	227	149	2.66	109
COSPEC	9/22	1645-1736	5	3441	389	291	209	3.48	109
Lidar	9/22	1629-1748	8	3162	251	230	152	2.75	112
COSPEC	9/23	1119-1215	4	2833	250	235	75	1.51	28
Lidar	9/23	1131-1214	16	2958	191	173	170	3.27	30
COSPEC	9/23	1524-1609	6	2734	196	159	74	1.56	32
Lidar	9/23	1530-1609	14	2979	209	128	283	5.44	30
COSPEC	10/28	1607-1642	7	2221	388	320	140	3.61	124
Lidar	10/28	1606-1632	4	3010	215	168	130	2.48	120

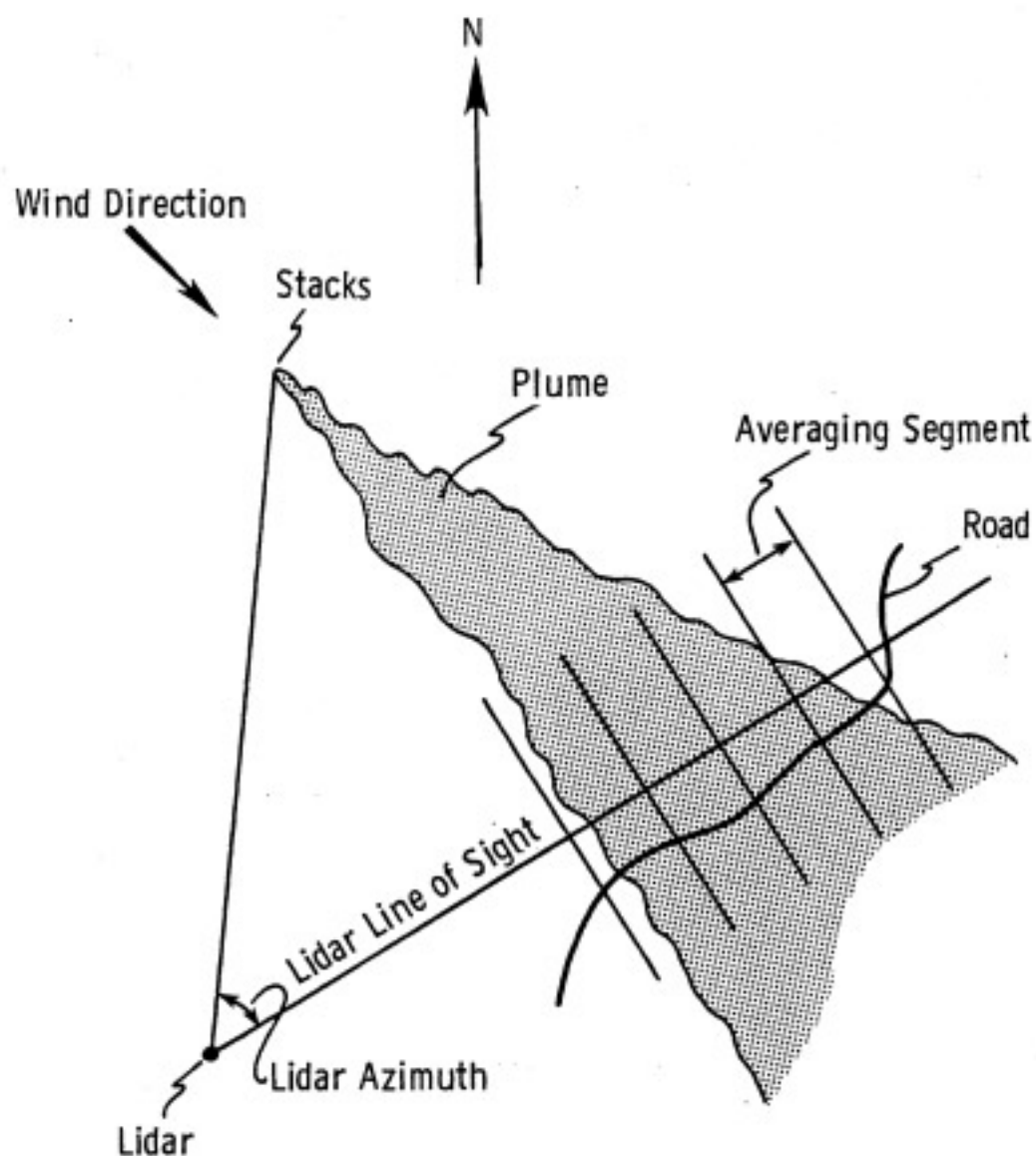


Figure B-1. Plan view of plume and measurement geometry.



Sept. 22, 1976

Mobile Van 1557 - 1638 ; 1645 - 1736

Lidar 1558 - 1619 ; 1629 - 1748

Mobile Van Measurement Route

Stacks

Lidar Line of Sight

Lidar

1 km

Figure B-2. Measurement route and lidar scan geometry for September 22, 1976.

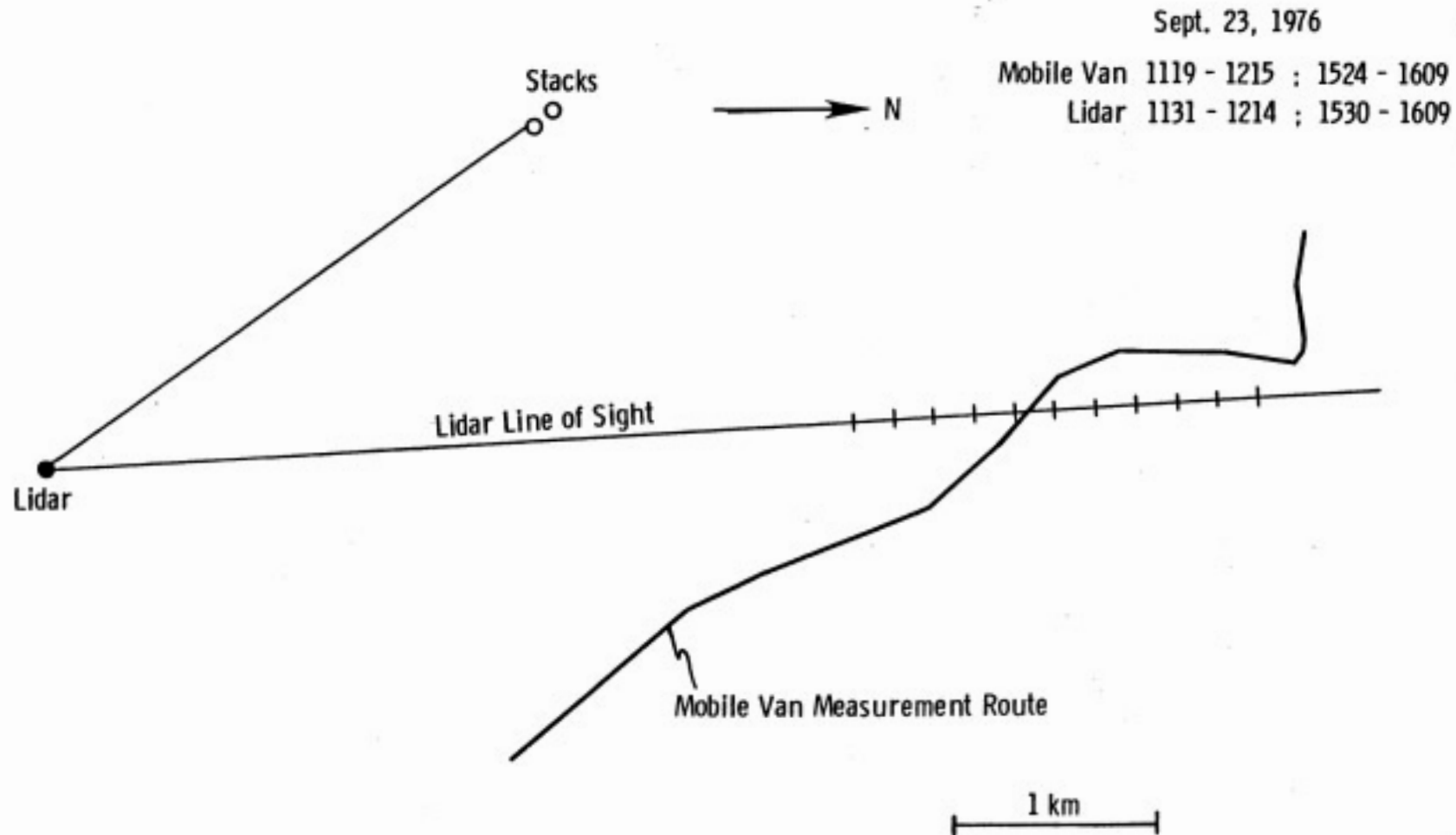


Figure B-3. Measurement route and lidar scan geometry for September 23, 1976.

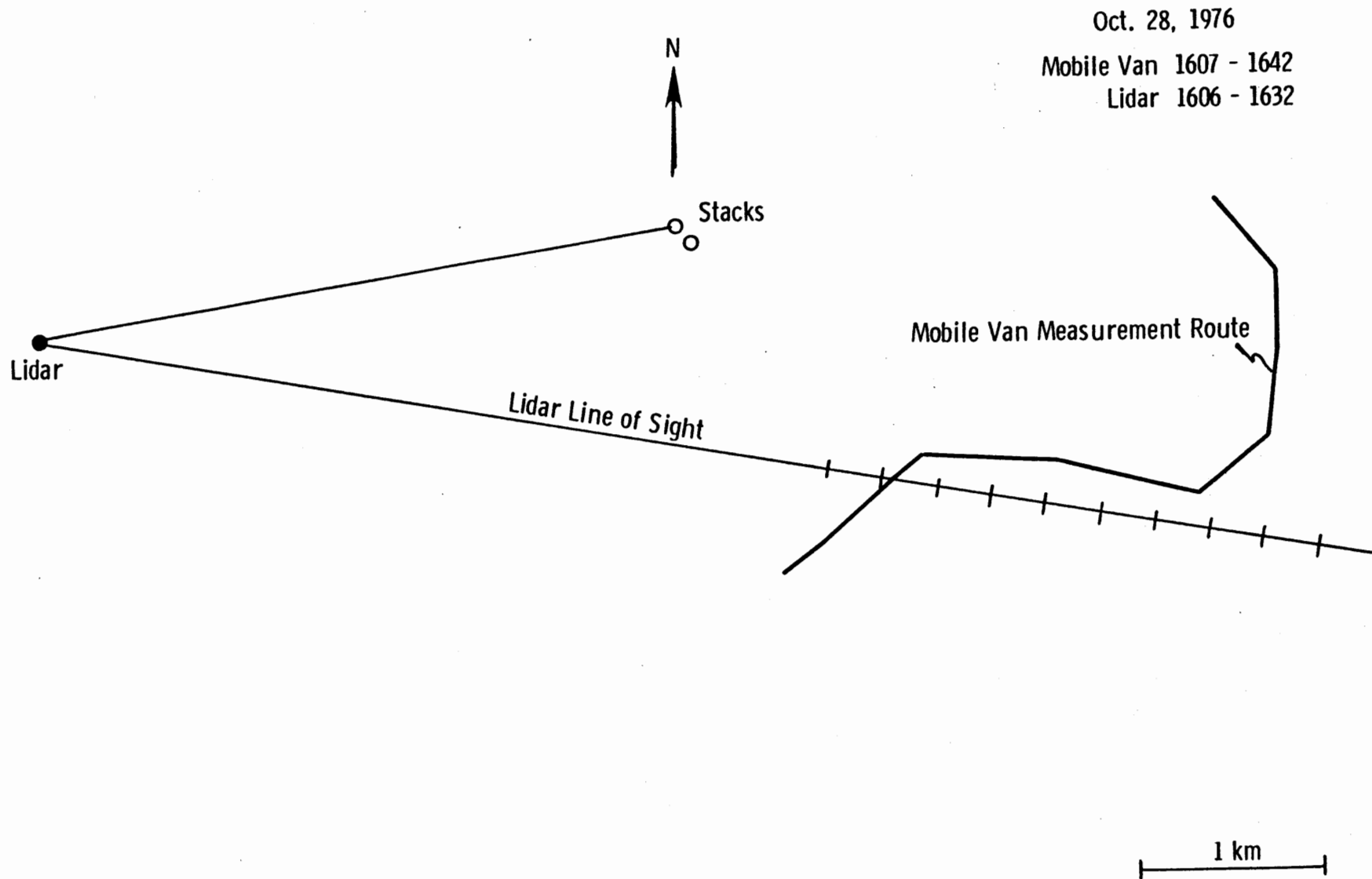


Figure B-4. Measurement route and lidar scan geometry for October 28, 1976.

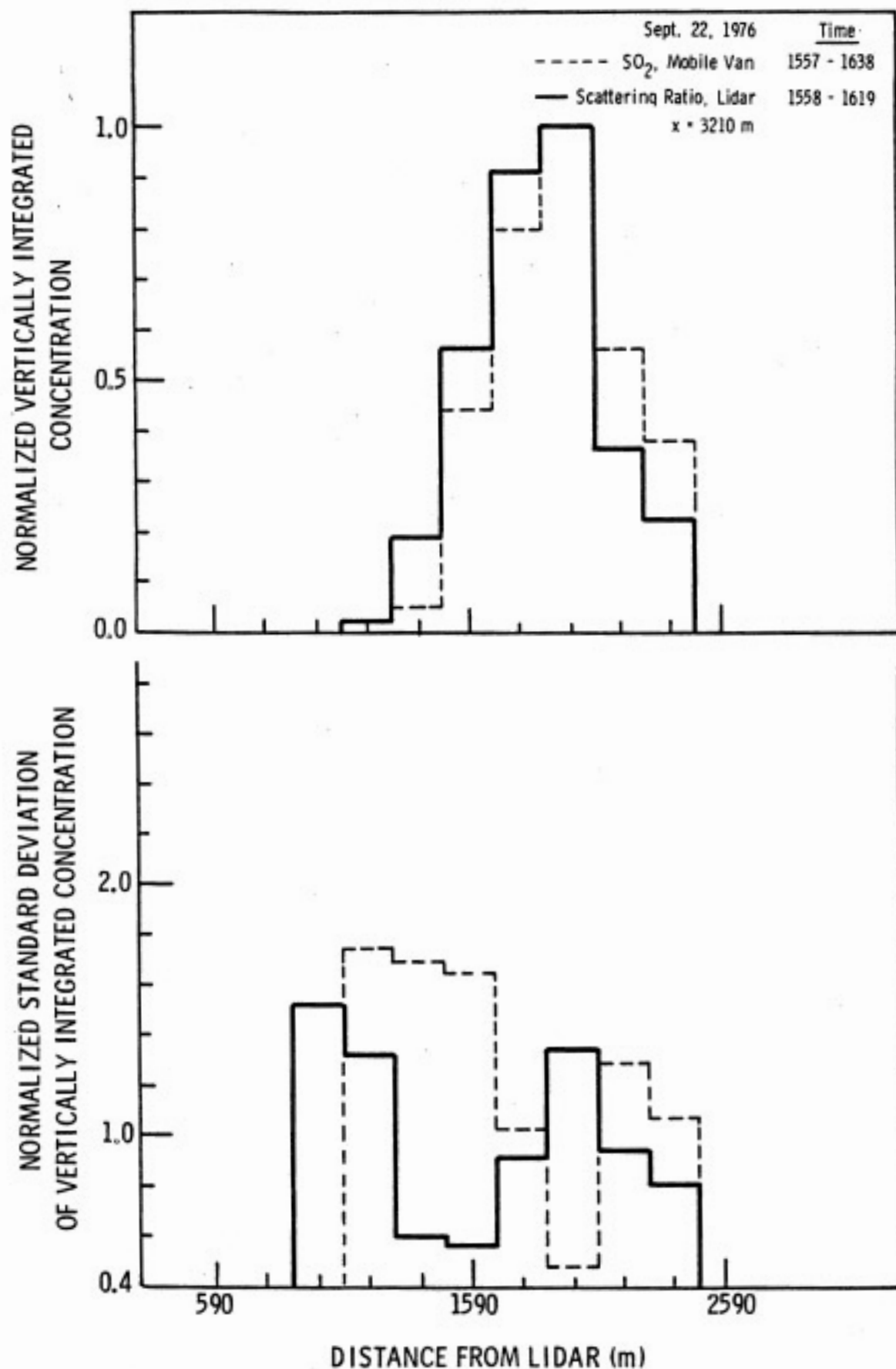


Figure B-5. Normalized average concentrations and standard deviations by crosswind segment.

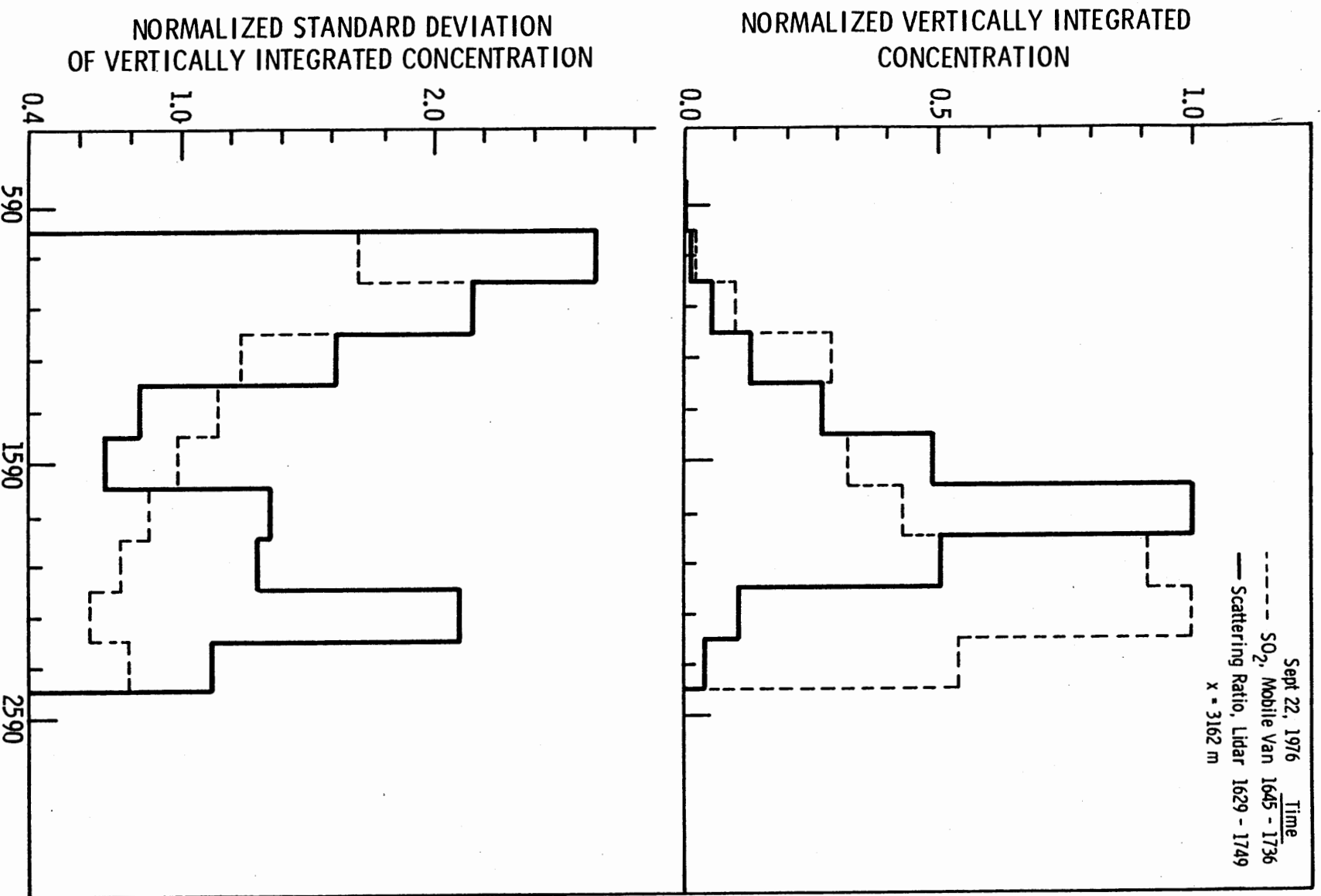


Figure B-6. Normalized average concentrations and standard deviations by crosswind segment.

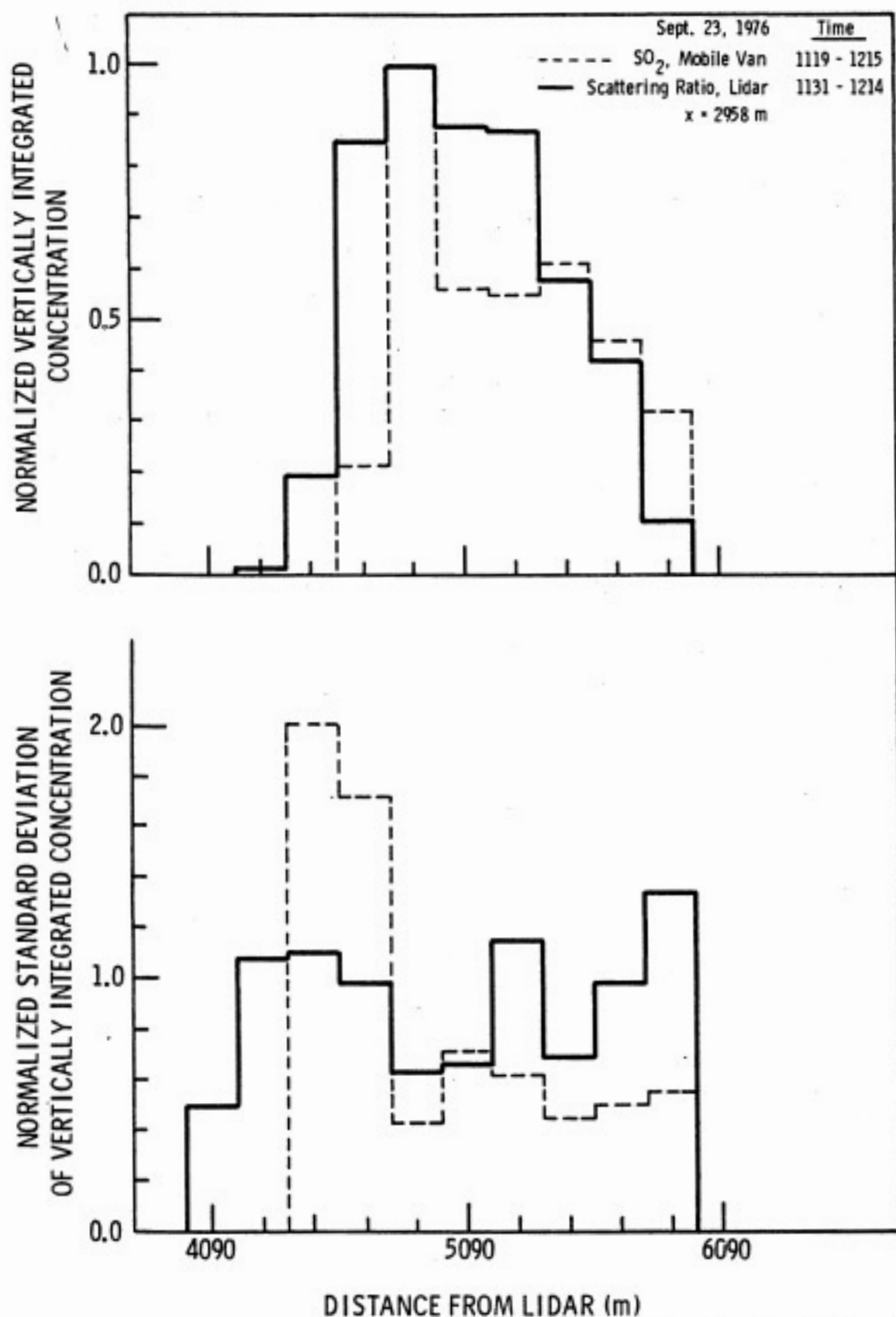


Figure B-7. Normalized average concentrations and standard deviations by crosswind segment.

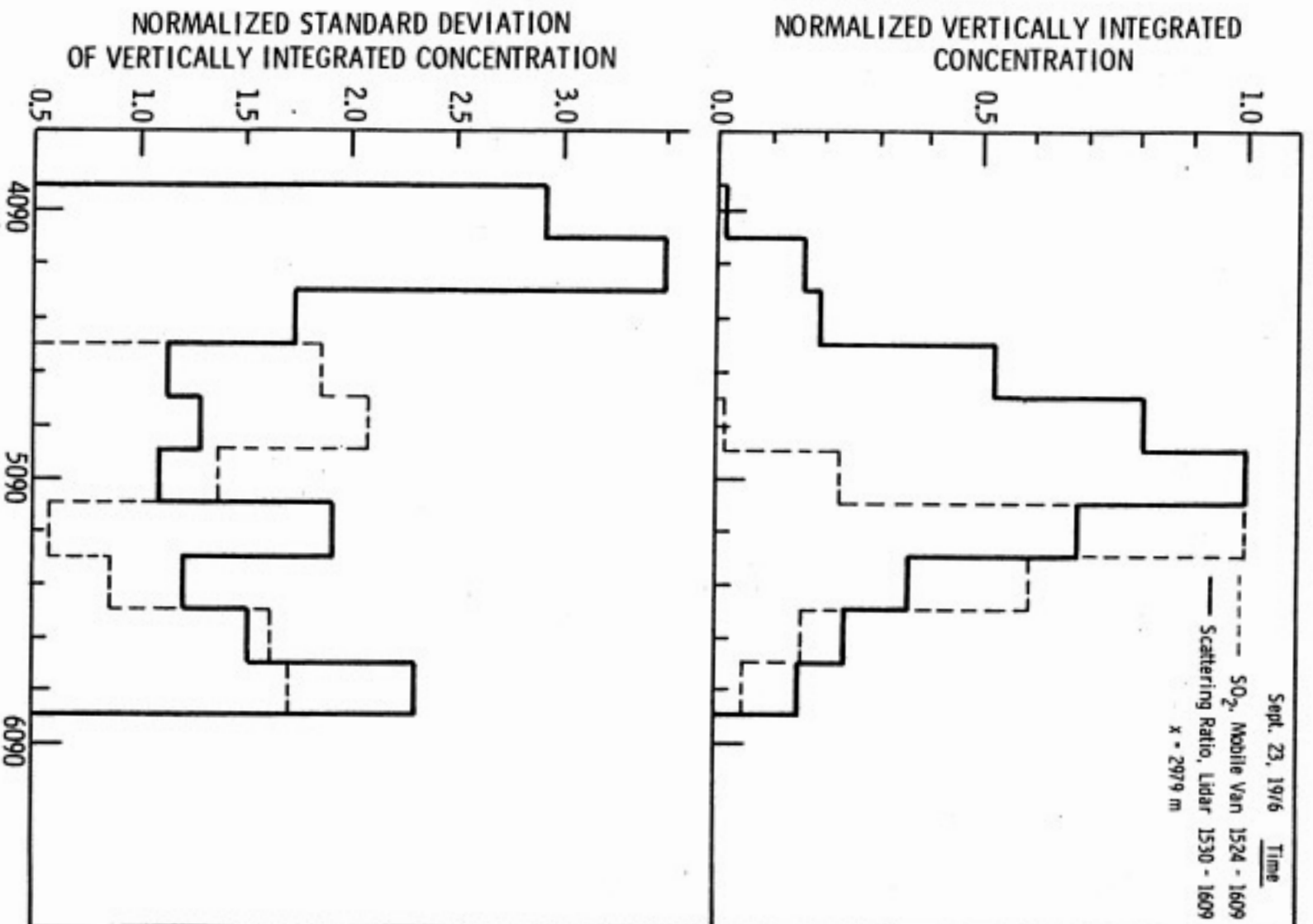


Figure B-8. Normalized average concentrations and standard deviations by crosswind segment.

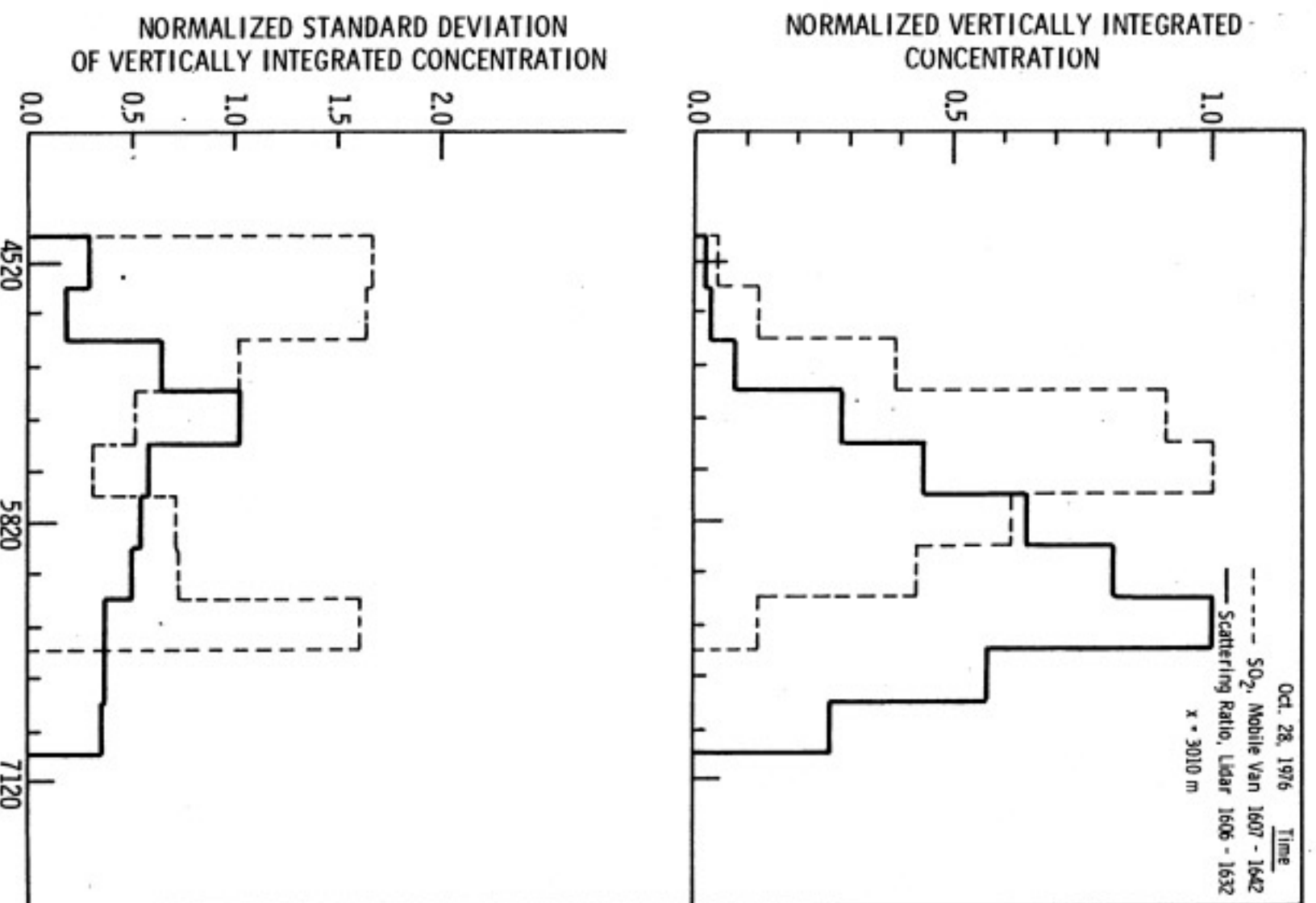


Figure B-9. Normalized average concentrations and standard deviations by crosswind segment.